ARTICLE IN PRESS

Pergamon

Available online at www.sciencedirect.com

SCIENCE DIRECT®

Acta Materialia XX (2003) XXX–XXX

Acta MATERIALIA

www.actamat-journals.com

Depth-sensing instrumented indentation with dual sharp indenters

N. Chollacoop, M. Dao, S. Suresh *

Department of Materials Science and Engineering, Massachusetts Institute of Technology, Room 8-309, 77 Massachusetts Avenue, Cambridge, MA 02139-4307, USA

Received 27 November 2002; accepted 13 March 2003

Abstract

A methodology for interpreting instrumented sharp indentation with dual sharp indenters with different tip apex angles is presented by recourse to computational modeling within the context of finite element analysis. The forward problem predicts an indentation response from a given set of elasto-plastic properties, whereas the reverse analysis seeks to extract elasto-plastic properties from depth-sensing indentation response by developing algorithms derived from computational simulations. The present study also focuses on the uniqueness of the reverse algorithm and its sensitivity to variations in the measured indentation data in comparison with the single indentation analysis on Vickers/Berkovich tip (Dao et al. Acta Mater 49 (2001) 3899). Finite element computations were carried out for 76 different combinations of elasto-plastic properties representing common engineering metals for each tip geometry. Young's modulus, E, was varied from 10 to 210 GPa; yield strength, σ_y, from 30 to 3000 MPa; and strain hardening exponent, n, from 0 to 0.5; while the Poisson's ratio, ν, was fixed at 0.3. Using dimensional analysis, additional closed-form dimensionless functions were constructed to relate indentation response to elasto-plastic properties for different indenter tip geometries (i.e., 50°, 60° and 80° cones). The representative plastic strain ε_r, as defined in Dao et al. (Acta Mater 49 (2001) 3899), was constructed as a function of tip geometry in the range of 50° and 80°. Incorporating the results from 60° tip to the single indenter algorithms, the improved forward and reverse algorithms for dual indentation can be established. This dual indenter reverse algorithm provides a unique solution of the reduced Young's modulus E^*, the hardness p_{ave} and two representative stresses (measured at two corresponding representative strains), which establish the basis for constructing power-law plastic material response. Comprehensive sensitivity analyses showed much improvement of the dual indenter algorithms over the single indenter results. Experimental verifications of these dual indenter algorithms were carried out using a 60° half-angle cone tip (or a 60° cone equivalent 3-sided pyramid

* Corresponding author. Tel.: +1-617-253-3320; fax: +1-617-253-0868.

E-mail address: ssuresh@mit.edu (S. Suresh).

doi:10.1016/S1359-6454(03)00186-1

tip) and a standard Berkovich indenter tip for two materials: 6061-T6511 and 7075-T651 aluminum alloys. Possible extensions of the present results to studies involving multiple indenters are also suggested.

Keywords: Indentation; Representative strain; Dual indenter geometries; Mechanical properties; Finite element simulation

1. Introduction

Depth-sensing instrumented indentation, where the indenter penetration force P can be continuously monitored as a function of the depth of penetration h into a substrate during both loading and unloading, has been a topic of considerable experimental and theoretical studies during the past two decades (e.g., [1–15]). Methods to extract material properties from instrumented indentation response have been investigated in a number of studies (e.g., [1,4,6,12,13,16–23]).

The underlying theoretical framework of plastic indentation dates back to the work by Hill et al. [25], who developed a self-similar solution for spherical indentation of a power law plastic material. Extending such an approach to sharp (Berkovich and Vickers) indentation, elastic–plastic analyses of Berkovich and Vickers indentation have been reported within the context of small-strain finite element simulations [19,26]. Extensions of these computational models included attempts to extract elasto-plastic properties from a single indentation load–displacement curve [17,21,22]. With the application of dimensional analysis to the computational results of large deformation sharp indentation, correlations between elasto-plastic properties and indentation response have also been proposed for bulk [1,12,13,20] and coated [24] material systems.

Our previous study [1] of instrumented indentation involving a single sharp indenter established a set of dimensionless functions, which took into account the pile-up/sink-in effects and finite strain beneath the indenter. These functions were used to predict the indentation response from a given set of elasto-plastic properties (forward algorithms), and to extract the elasto-plastic properties from a given set of indentation data (reverse algorithms). A representative strain of ε_r=3.3% for a Berkovich or Vickers indenter (equivalent to a 70.3° cone) was identified with which the indentation loading curvature could be normalized independently of the material hardening exponent for a very wide range of elasto-plastic properties. For most common metallic systems, a single set of elasto-plastic properties was extracted from a single P–h curve. The accuracy of the analysis, however, was found to be sensitive to the small experimental errors [1]. Cheng and Cheng [20] and Venkatesh et al. [22] discussed the uniqueness issue and presented a number of computationally non-unique cases.

It is clear that two important fundamental issues remain which require further investigation:

1. Uniqueness of the reverse analysis for the range of material properties examined; and
2. The accuracy and sensitivity of the reverse analysis.

In this paper, these issues will be addressed within the context of dual sharp indentation, continuum analysis and experimental observations.

2. Framework for analysis

2.1. Problem formulation and nomenclature

Fig. 1(a) schematically shows the typical P–h response of an elasto-plastic material to sharp indentation. The loading response is governed by Kick's Law,

$$P = Ch^2 \quad (1)$$

where C is the loading curvature. At the maximum depth h_m, the indentation load P_m makes a projected contact area of A_m. The average contact pressure is thus defined as $p_{ave} = P_m/A_m$, commonly referred as the hardness of the indented

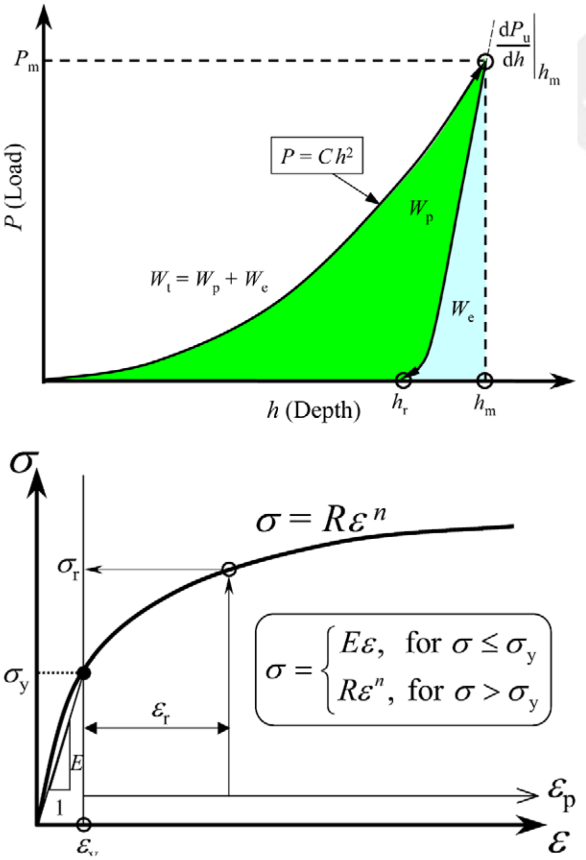

Fig. 1. (a) Schematic illustration of a typical P–h response of an elasto-plastic material to instrumented sharp indentation. (b) The power law elasto-plastic stress–strain behavior used in the current study.

material, in accordance with the standard for commercially available indenter. Upon unloading, the initial unloading slope is defined as $\frac{dP_u}{dh}\Big|_{h_m}$, where P_u is the unloading force. At the complete unloading, the residual depth is h_r. The area under the loading portion is defined as the total work W_t; the area under the unloading portion is defined as the recovered elastic work W_e; and the area enclosed by the loading and unloading portions is defined as the residual plastic work $W_p = W_t - W_e$.

Fig. 1(b) schematically shows the typical stress–strain response of power law material, which, to a good approximation, can be used for many pure and alloyed engineering metals. The elasticity follows Hook's law, whereas the plasticity follows von Mises yield criterion and power law hardening. True stress and true strain are related via the following equation:

$$\sigma = \begin{cases} E\varepsilon & \text{for } \sigma \le \sigma_y \\ R\varepsilon^n & \text{for } \sigma > \sigma_y \end{cases} \tag{2}$$

where E is the Young's modulus, R a strength coefficient, n the strain hardening exponent and σ_y the initial yield stress at zero offset strain. In the plastic region, true strain can be further decomposed to strain at yield and true plastic strain: $\varepsilon = \varepsilon_y + \varepsilon_p$. For continuity at yielding, the following condition must hold.

$$\sigma_y = E\varepsilon_y = R\varepsilon_y^n \tag{3}$$

Thus when $\sigma > \sigma_y$, Eqs. (2) and (3) yield

$$\sigma = \sigma_y\left(1 + \frac{E}{\sigma_y}\varepsilon_p\right)^n. \tag{4}$$

A comprehensive framework using dimensional analysis to extract closed form universal functions was developed earlier [1]. A representative plastic strain ε_r was identified as a strain level which allows for the construction of a dimensionless description of indentation loading response, independent of strain hardening exponent n; ε_r=3.3% for Berkovich, Vickers or 70.3° apex-angle cone tip. It was also found that for most cases, three independent quantities—C, $\frac{dP_u}{dh}\Big|_{h_m}$ and $\frac{h_r}{h_m}$—obtained from a single P–h curve are sufficient to uniquely determine the indented material's elasto-plastic properties under certain ranges of validity (see Table 6 of [1]). Although the estimation of σ_y and n in certain ranges could be prone to considerable sensitivity from a variation in these three P–h characteristics (see Table 7 of [1]), a reverse analysis algorithm proposed in [1] predicts stress at representative strain, $\sigma_{0.033}$, robustly.

It is expected that, with different indenter geometries (i.e., different apex angles), the representative strain would be different (e.g., ε_r=$\varepsilon_r(\theta)$). In fact, a ±2° variation in apex angle can result in a ±20% change in loading curvature C (see Fig. 12 of [1]). This observation suggests a possibility of determining σ_y and n more precisely using dual indenter geometries (two representative stresses). An additional representative stress σ_r can be identified from a loading curvature of a P–h curve using a second indenter of which its tip geometry is different from Berkovich/Vickers. The question remains whether two P–h curves from two different indenter tips can yield unique solution for a broader range of material's elasto-plastic properties with improved accuracy than previously demonstrated with a single indentation.

2.2. Dimensional analysis and universal functions

For a sharp indenter of apex angle θ, the load required to penetrate into a power law elasto-plastic solid (E, ν, σ_y and n) can be written as

$$P = P(h,E^*,\sigma_y,n,\theta), \tag{5}$$

where

$$E^* = \left[\frac{1-\nu^2}{E} + \frac{1-\nu_i^2}{E_i}\right]^{-1} \tag{6}$$

is reduced Young's modulus, commonly introduced [27] to include elasticity effect (E_i, ν_i) of an elastic indenter. Define σ_r as the stress at the representative strain ε_r in Eq. (4); Eq. (5) can be rewritten as

$$P = P(h,E^*,\sigma_r,n,\theta) \tag{7}$$

Using dimensional analysis, Eq. (7) becomes

$$P = \sigma_r h^2 \Pi_{1\theta}\left(\frac{E^*}{\sigma_r},n,\theta\right), \tag{8a}$$

and from Eq. (1),

$$C = \frac{P}{h^2} = \sigma_r \Pi_{1\theta}\left(\frac{E^*}{\sigma_r},n,\theta\right). \tag{8b}$$

where $\Pi_{1\theta}$ is a dimensionless function.

A complete set of universal dimensionless functions for a single indenter is listed in Appendix A (Eqs. (A.1)–(A.6)) for an apex angle of 70.3° (Berkovich and Vickers equivalent). In the current study, $\Pi_{1\theta}$ functions at different apex angles (e.g., 50°, 60° or 80°) will be constructed. The original algorithms in [1] can be modified to accurately predict the P–h response from known elasto-plastic properties (forward algorithms) and to systematically and uniquely extract the indented material's elasto-plastic properties from two sets of P–h data of two different indenter geometries (reverse algorithms).

2.3. Computational model

It is generally known that an axisymmetric two-dimensional finite element model can be used to capture the result of a full three-dimensional model as long as the projected area/depth of the two models are equivalent. Computations were performed using the general purpose finite element package ABAQUS [28]. Fig. 2(a) schematically shows the conical indenter, where

θ = the included half angle of the indenter
h_m= the maximum indentation depth
a_m= the contact radius measured at h_m
A_m= the true projected contact area with pile-up or sink-in effects taken into account.

For both Berkovich and Vickers indenters, the corresponding apex angle θ of the equivalent cone was chosen as 70.3°. Fig. 2(b) shows the mesh design for the axisymmetric analysis. The indented solid spanned over a hundred times contact radius to ensure semi-infinite boundary condition. The model comprised of 8100 four-noded, bilinear axisymmetric quadrilateral elements with a fine mesh near the contact region and a gradually coarser mesh further away to ensure numerical accuracy. At the maximum load, the minimum number of contact elements in the contact zone was no less than 12 in each FEM computation. The mesh was well-tested for convergence and was determined to be insensitive to far-field boundary conditions. In all finite element computations, the indenter was modeled as a rigid body; the contact was modeled as frictionless; and large deformation FEM computations were performed.

2.4. Comparison of experimental and computational results

Two aluminum alloys (6061-T6511 and 7075-T651) were prepared, as described elsewhere [1],

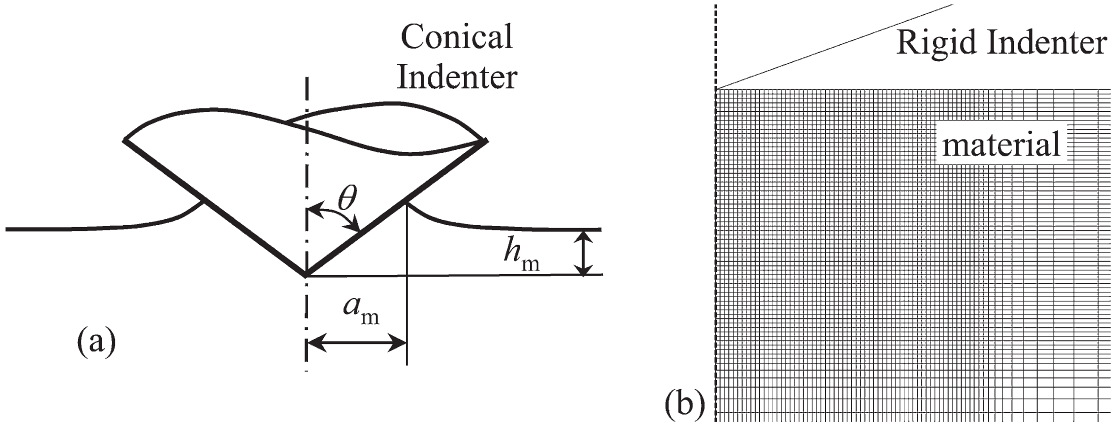

Fig. 2. Computational modeling of instrumented sharp indentation. (a) Schematic drawing of the conical indenter, (b) mesh design for axisymmetric finite element calculations

for indentation using a Berkovich tip and a second indenter tip with different geometry. The specimens were indented on a commercial nanoindenter (MicroMaterials, Wrexham, UK) with the Berkovich, 60° cone and 60° cone equivalent 3-sided pyramid[1] at a loading/unloading rate of approximately 4.4 N/min. For the Berkovich tip, the maximum loads for both aluminum alloys were 3 N with a repetition of six tests. For the other two indenter tips, the Al6061-T6511 specimens were indented to 1.8 and 2.7 N with a repetition of 3 and 10 tests, respectively; whereas the Al7075-T651 specimens were indented to 3 N with a repetition of six tests. From all the tests, the data were repeatable. For comparison with the single indentation results, the Berkovich indentation data of Al6061-T6511 specimens examined in the current study were taken directly from [1].

Fig. 3 shows the typical indentation response of the 6061-T6511 aluminum specimens under Berkovich and 60° cone indenter tips, superimposed with the corresponding finite element computations. Fig. 4 shows the same for the 7075-T651 aluminum. Using experimental uniaxial compression (see Fig. 4 of [1]) as an input for the simulation, the resulting *P*–*h* curves agree well with the experimental curves, as demonstrated in Figs. 3 and 4.

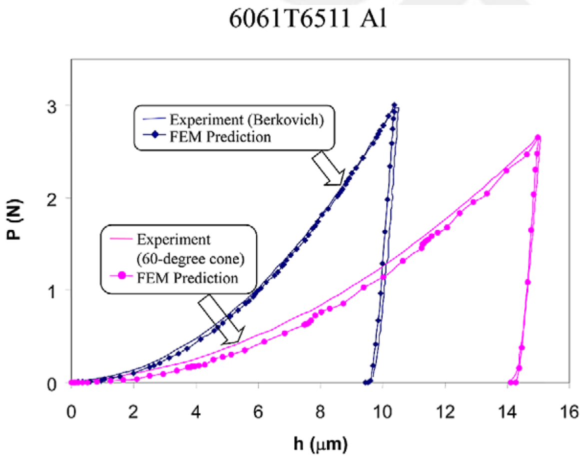

Fig. 3. Experimental (Berkovich and 60° cone tips) versus computational indentation responses of both the 6061-T6511 aluminum specimens.

3. Computational results

A comprehensive parametric study of 76 cases was conducted (see Appendix B for a complete list of parameters) representing the range of parameters of mechanical behavior found in common engineering metals. Values of Young's modulus *E*

[1] The 60° cone equivalent 3-sided pyramid is designed such that its projected contact area/depth equals to that of 60° cone.

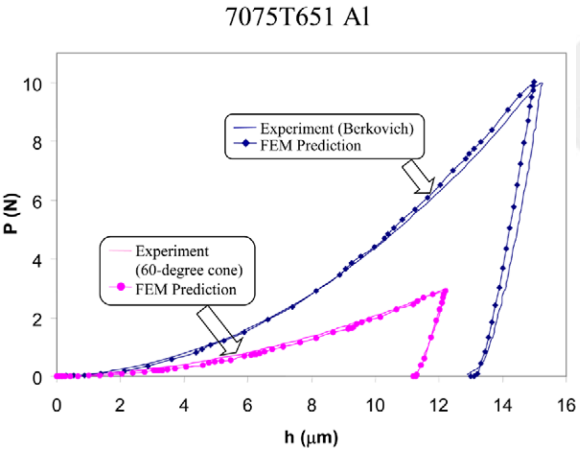

Fig. 4. Experimental (Berkovich and 60° cone tips) versus computational indentation responses of both the 7075-T651 aluminum specimens.

ranged from 10 to 210 GPa, yield strength σ_y from 30 to 3000 MPa, strain hardening exponent n from 0 to 0.5, and Poisson's ratio ν was fixed at 0.3. The axisymmetric finite element model was used to obtain computational results, unless otherwise specified.

The dimensionless functions $\Pi_{1\theta}$ for different apex angles (e.g., 50°, 60° or 80°) were constructed in addition to the $\Pi_{1\theta}$ function at 70.3° angle (Berkovich and Vickers equivalent) presented earlier [1]. It is noted that the apex angle of 60° is commonly used in commercial indenters for scanning the surface profile or performing indentation tests. The second indenter tip geometry is chosen to be 60° cone.

3.1. *Representative strain and dimensionless function Π_1 as a function of indenter geometry*

The first dimensionless function of interest is $\Pi_{1\theta}$ in Eq. (8a,b). Using subscript "*a*" to denote $\theta = 70.3°$ in Eq. (8a,b), it follows that

$$\Pi_{1a}\left(\frac{E^*}{\sigma_{r,a}}, n, \theta = 70.3°\right) = \frac{C_a}{\sigma_{r,a}} \tag{9}$$

It was found in [1] that for $\theta = 70.3°$ a representative strain of 0.033 could be identified, such that a polynomial function $\Pi_{1a}\left(\frac{E^*}{\sigma_{0.033}}\right) = \frac{C_a}{\sigma_{0.033}}$ fits all 76 data points within a ±2.85% error (see Appendix A for a complete listing of the function). It is worth noting that the corresponding dimensionless function Π_{1a} normalized with respect to $\sigma_{0.033}$ was found to be independent of the strain hardening exponent n.

Following the same procedure, one can identify the $\Pi_{1\theta}$ functions with different apex angles (i.e., different tip geometries). Three additional angles were studied here. For $\theta = 60°$, a representative strain of 0.057 could be identified, where a closed-form function $\Pi_{1b}\left(\frac{E^*}{\sigma_{0.057}}\right) = \frac{C_b}{\sigma_{0.057}}$ (see Appendix A for a complete listing of the function) fits all 76 data points within a ±2.51% error; here the subscript "*b*" is used to denote the case for $\theta = 60°$. For $\theta = 80°$, a representative strain of 0.017 could be identified, where a closed form function $\Pi_{1c}\left(\frac{E^*}{\sigma_{0.017}}\right) = \frac{C_c}{\sigma_{0.017}}$ (see Appendix A for a complete listing of the function) fits all 76 data points within a ±2.71% error; here the subscript "*c*" is used to denote the case for $\theta = 80°$. For $\theta = 50°$, a representative strain of 0.082 could be identified, where a closed-form function $\Pi_{1d}\left(\frac{E^*}{\sigma_{0.082}}\right) = \frac{C_d}{\sigma_{0.082}}$ (see Appendix A for a complete listing of the function) fits all 76 data points within a ±2.49% error; here the subscript "*d*" is used to denote the case for $\theta = 50°$. The representative strain can be correlated with the half tip angle via a simple linear function (see Fig. 5(a)).

$$\varepsilon_r(\theta) = -2.185 \times 10^{-3}\theta + 0.1894 \quad \text{for } \theta \text{ in degree} \tag{10a}$$

or a more accurate quadratic function, within ±1.63% error,

$$\varepsilon_r(\theta) = 2.397 \times 10^{-5}\theta^2 - 5.311 \times 10^{-3}\theta + 0.2884 \quad \text{for } \theta \text{ in degree} \tag{10b}$$

To extend the capability of the present dual indentation algorithm, the choice for the second indenter geometry can be chosen between 50° and 80°. By correlating the coefficients in Eqs. (A.1), (A.7), (A.8) and (A.9) with apex angle θ,

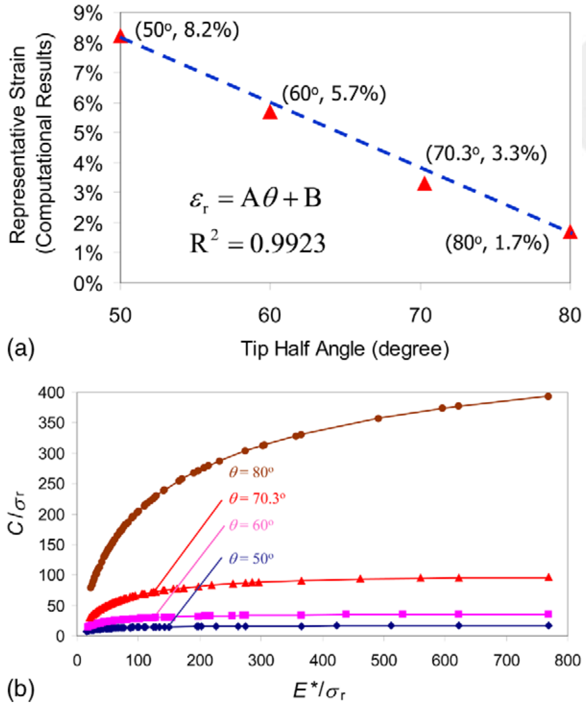

Fig. 5. (a) A relationship between representative strain and indenter apex angle. (b) A generalized dimensionless function $\Pi_{1\theta}$ for $\theta = 50°, 60°, 70.3°$ and $80°$.

$\Pi_{1\theta}\left(\frac{E^*}{\sigma_{\varepsilon_r}},\theta\right) = \frac{C_\theta}{\sigma_{\varepsilon_r}}$ (see Appendix A for a complete listing of the function) fits all $4 \times 76 = 304$ data points within a ±3% error, as shown in Fig. 5(b).

3.2. Forward analysis algorithms

In the following sections, the dual indenter geometries of the 70.3° and 60° pair are examined. The forward analysis leads to prediction of the P–h response from known elasto-plastic properties. Following the procedure outlined in [1], an updated forward analysis algorithm for generalized dual indentation is shown in Fig. 6. The complete prediction of P–h response can be readily constructed for $\theta = 70.3°$ using dimensionless functions Π_{1a} to Π_{6a}, while the prediction of loading curvature can be obtained for any $\theta \in [50°,80°]$ using $\Pi_{1\theta}$.

To verify the accuracy of the proposed algorithms, uniaxial compression and Berkovich indentation experiments were conducted in two well-characterized materials: 6061-T6511 aluminum and 7075-T651 aluminum (see Fig. 4 of [1]). Additional indentation experiments using a different tip geometry (either a 60° cone or an equivalent 3-sided pyramid) were performed on both 6061-T6511 and 7075-T651 aluminum samples. The mechanical property values used in the forward analysis were obtained directly from Table 3 of [1], where (E, ν, σ_y, n) are (66.8 GPa, 0.33, 284 MPa, 0.08) and (70.1 GPa, 0.33, 500 MPa, 0.0122) for Al6061-T6511 and Al7075-T651, respectively. Tables 1–3 list the predictions from the forward analysis (using Π_{1a} to Π_{6a} and Π_{1b}) for 6061-T6511 aluminum specimens, along with the values extracted from the Berkovich indentation, the 60° cone indentation, and the 60° cone equivalent 3-sided pyramid indentation experiments, respectively. Tables 4 and 5 list the predictions from the forward analysis (using Π_{1a} to Π_{6a} and Π_{1b}) for 7075-T651 aluminum specimens, along with the values extracted from the Berkovich indentation and the 60° cone equivalent 3-sided pyramid indentation experiments, respectively. From Tables 1–5, it is evident that the present forward analysis results are in good agreement with the experimental P–h curves.

3.3. Reverse analysis algorithms

Since a single P–h curve is sufficient for estimation of the elasto-plastic properties, the use of two complete P–h curves would give redundant information. Therefore, there are many possible ways to construct the reverse analysis algorithm; however, the most reliable path is presented here. The proposed reverse algorithm utilizes a complete P–h curve obtained under Berkovich or Vickers indenter and a loading portion of a second P–h curve under a conical indenter of apex angle $\theta \in [50°,80°]$ (or its equivalent 3-sided pyramid). In the present study, $\theta = 60°$ is chosen. The dimensionless functions Π_{1a} to Π_{6a} and $\Pi_{1\theta}$ allow us to construct an improved reverse algorithm. A set of the dual indentation reverse analysis algorithms is shown in Fig. 7.

To verify the dual indentation reverse algorithms, six Berkovich indentation curves shown in

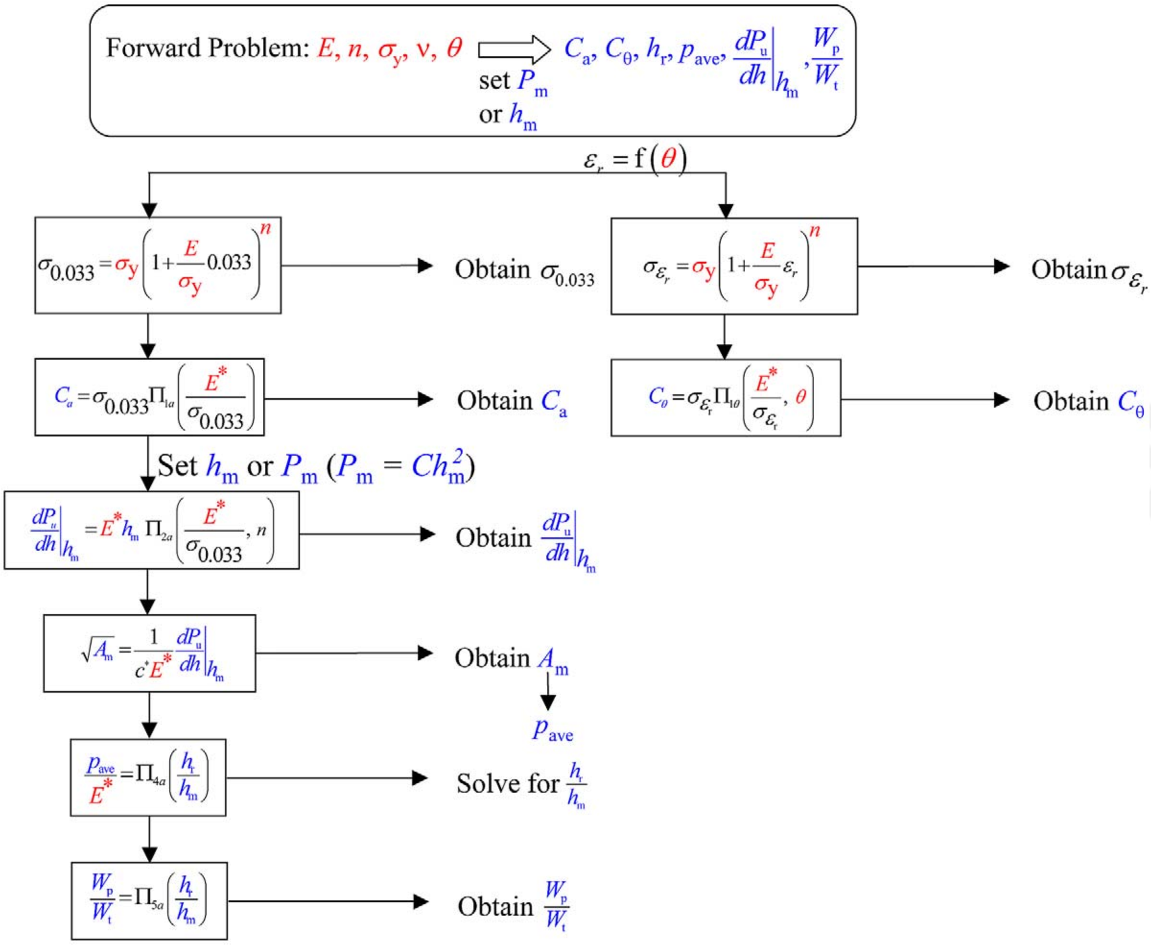

Fig. 6. Dual indentation forward analysis algorithms.

Table 1 and three 60° cone indentation curves shown in Table 2 from 6061-T6511 aluminum specimens were first analyzed (using Π_{1a} to Π_{6a} and Π_{1b}). Table 6 shows the dual indentation results, along with the single indentation results from [1]. In the reverse analyses, each case comprises one set of Berkovich indentation parameters shown in Table 1 and an average loading curvature C_b shown in Table 2 for the 60° cone indentation.

Additional verification for the dual indentation algorithms was performed on 7075-T651 aluminum specimens. Six Berkovich indentation *P–h* curves shown in Table 4 and six 60° cone equivalent 3-sided pyramid indentation curves shown in Table 5 were analyzed (using Π_{1a} to Π_{6a} and Π_{1b}). Table 7 shows the dual indentation results, along with the single indentation results. In the reverse analyses, each case comprises one set of Berkovich indentation parameters shown in Table 4 and an average loading curvature C_b shown in Table 5 for the 60° cone equivalent 3-sided pyramid indentation.

According to the flow chart shown in Fig. 7, the predictions of E^* and $\sigma_{0.033}$ by the dual indentation algorithm should yield the similar accuracy to those by the single indentation algorithm.

From Tables 6 and 7, it is clear that the proposed reverse algorithms yield accurate estimates of $\sigma_{0.033}$, $\sigma_{0.057}$ and E^*, and give reasonable estimates of σ_y (especially after taking an average from the

Table 1
Forward analysis on Al 6061-T6511 for Berkovich indentation experiments (max. load = 3 N) [1]

Al 6061-T6511	C_a (GPa)	%error C_a[a]	$\left.\frac{dP_u}{dh}\right\|_{h_m}$ (kN/m)	%error $\left.\frac{dP_u}{dh}\right\|_{h_m}$	W_p/W_t	%error W_p/W_t
Test A1	27.4	−1.6	4768	1.6	0.902	0.8
Test A2	28.2	1.2	4800	2.3	0.905	1.2
Test A3	27.2	−2.4	4794	2.2	0.904	1.1
Test A4	27.3	−2.2	4671	−0.4	0.889	−0.6
Test A5	27.0	−3.2	4762	1.5	0.889	−0.6
Test A6	27.6	−0.9	4491	−4.2	0.891	−0.4
Average	27.4		4715		0.896	
Forward prediction (assume $\nu = 0.33$ and Berkovich $c*$)	27.9		4691		0.894	
STDEV[b]	0.6		110.9		0.007	
STDEV/$X_{prediction}$	2.1%		2.4%		0.8%	

[a] All errors were computed as $X_{test}-X_{prediction}/X_{prediction}$, where X represents a variable.

[b] STDEV $= \sqrt{\frac{1}{N}\Sigma_{i=1}^{N}(X_{test}-X_{prediction})^2}$, where X represents a variable.

Table 2
Forward analysis on Al 6061-T6511 for 60° cone experiments (max. load = 1.8 N)

Al 6061-T6511	C_b (GPa)	%error C_b[a]
Test B1c	11.27	0.0
Test B2c	11.23	−0.4
Test B3c	11.32	0.5
Average	11.27	
Forward prediction (60° cone)	11.27	
STDEV[b]	0.04	
STDEV/$X_{prediction}$	0.3%	

[a] All errors were computed as $X_{test}-X_{prediction}/X_{prediction}$, where X represents a variable.

[b] STDEV $= \sqrt{\frac{1}{N}\Sigma_{i=1}^{N}(X_{test}-X_{prediction})^2}$, where X represents a variable.

Table 3
Forward analysis on Al 6061-T6511 for 60° cone equivalent 3-sided pyramid indentation experiments (max. load = 1.8 N)

Al 6061-T6511	C_b (GPa)	%error C_b[a]
Test B1p	12.03	6.8
Test B2p	11.39	1.1
Test B3p	11.97	6.2
Average	11.80	
Forward prediction (60° cone equivalent 3-sided pyramid)	11.27	
STDEV[b]	0.60	
STDEV/$X_{prediction}$	5.4%	

[a] All errors were computed as $X_{test}-X_{prediction}/X_{prediction}$, where X represents a variable.

[b] STDEV $= \sqrt{\frac{1}{N}\Sigma_{i=1}^{N}(X_{test}-X_{prediction})^2}$, where X represents a variable.

six indentation results), which agree well with experimental uniaxial compression data. It is noted that changing the definition of σ_y to 0.1% or 0.2% (instead of 0%) offset strain would not affect the conclusions. According to the flow chart shown in Fig. 7, the improvement of the dual indentation algorithm over the single indentation algorithm reflects upon yield strength (and consequently strain hardening exponent) estimation, as clearly illustrated by comparing the first and last columns in Tables 6 and 7. This improved calculation of plastic properties is likely due to the fact that the second indenter geometry results in more accurate estimations of the second representative stress $\sigma_{0.057}$ at 5.7% plastic strain in addition to the representative stress $\sigma_{0.033}$ at 3.3% plastic strain.

Table 4
Forward analysis on Al 7075-T651 for Berkovich indentation experiments (max. load = 3 N)

Al 7075-T651	C (GPa)	%error C[a]	$\left.\frac{dP_u}{dh}\right\|_{h_m}$ (kN/m)	%error $\left.\frac{dP_u}{dh}\right\|_{h_m}$	W_p/W_t	%error W_p/W_t
Test A1	40.7	−7.1	3636	1.4	0.839	1.8
Test A2	42.6	−2.8	3637	1.4	0.831	0.9
Test A3	41.5	−5.5	3498	−2.5	0.829	0.6
Test A4	40.7	−7.2	3636	1.4	0.835	1.3
Test A5	40.8	−7.0	3566	−0.5	0.834	1.2
Test A6	41.2	−6.0	3600	0.4	0.831	0.8
Average	41.2		3595		0.833	
Forward prediction (assume $\nu = 0.33$ and Berkovich $c*$)	43.9		3585		0.824	
STDEV[b]	1.6		51.7		0.00956	
STDEV/$X_{prediction}$	3.7%		1.4%		1.2%	

[a] All errors were computed as $X_{test} - X_{prediction}/X_{prediction}$, where X represents a variable.

[b] STDEV = $\sqrt{\frac{1}{N}\Sigma_{i=1}^{N}(X_{test} - X_{prediction})^2}$, where X represents a variable.

Table 5
Forward analysis on Al 7075-T651 for 60° cone equivalent 3-sided pyramid indentation experiments (max. load = 3 N)

Al 7075-T651	C_b (GPa)	%error C_b[a]
Test B1p	17.41	−7.9
Test B2p	17.52	7.4
Test B3p	16.95	−10.4
Test B4p	17.75	−6.2
Test B5p	18.08	−4.4
Test B6p	17.90	−5.4
Average	17.60	
Forward prediction (60° cone equivalent 3-sided pyramid)	18.92	
STDEV[b]	1.37	
STDEV/$X_{prediction}$	7.2%	

[a] All errors were computed as $X_{test} - X_{prediction}/X_{prediction}$, where X represents a variable.

[b] STDEV = $\sqrt{\frac{1}{N}\Sigma_{i=1}^{N}(X_{test} - X_{prediction})^2}$, where X represents a variable.

4. Uniqueness of the dual indentation forward and reverse analysis

4.1. Uniqueness of the forward analysis

In order to verify the proposed forward algorithms, computational results from the 76 sets of elasto-plastic parameters were taken as input to predict the entire P–h responses of $\theta = 70.3°$ and the loading curvature for $\theta = 60°$. Each of the forward analyses resulted in a single set of output $\left(C_a, \frac{h_r}{h_m}, \left.\frac{dP_u}{dh}\right|_{h_m} \text{ and } C_b\right)$, which agrees well with the FEM-predicted P–h response.

4.2. Uniqueness of the reverse analysis

In order to verify the proposed reverse analysis algorithms, the 76 cases of the forward analysis (output) results were used as input to verify the uniqueness of the reverse analysis algorithms. All 76 cases resulted in a single, accurate re-construction of the initial elasto-plastic parameters. For the single indentation reverse algorithm in [1], two cases out of the same group of 76 cases resulted in no solution. The improvement over our previously proposed reverse algorithm [1] came from the fact that the dimensionless function Π_{2a} or Π_{3a}, which is not monotonic in n when $E^*/\sigma_{0.033} < 50$ for Π_{2a} or $\sigma_{0.033}/E^* < 0.005$ for Π_{3a}, is no longer used in the present reverse algorithm. Within the range of our current study, the dual indentation algorithm resolves the uniqueness problem.

Cheng and Cheng [20] discussed the non-

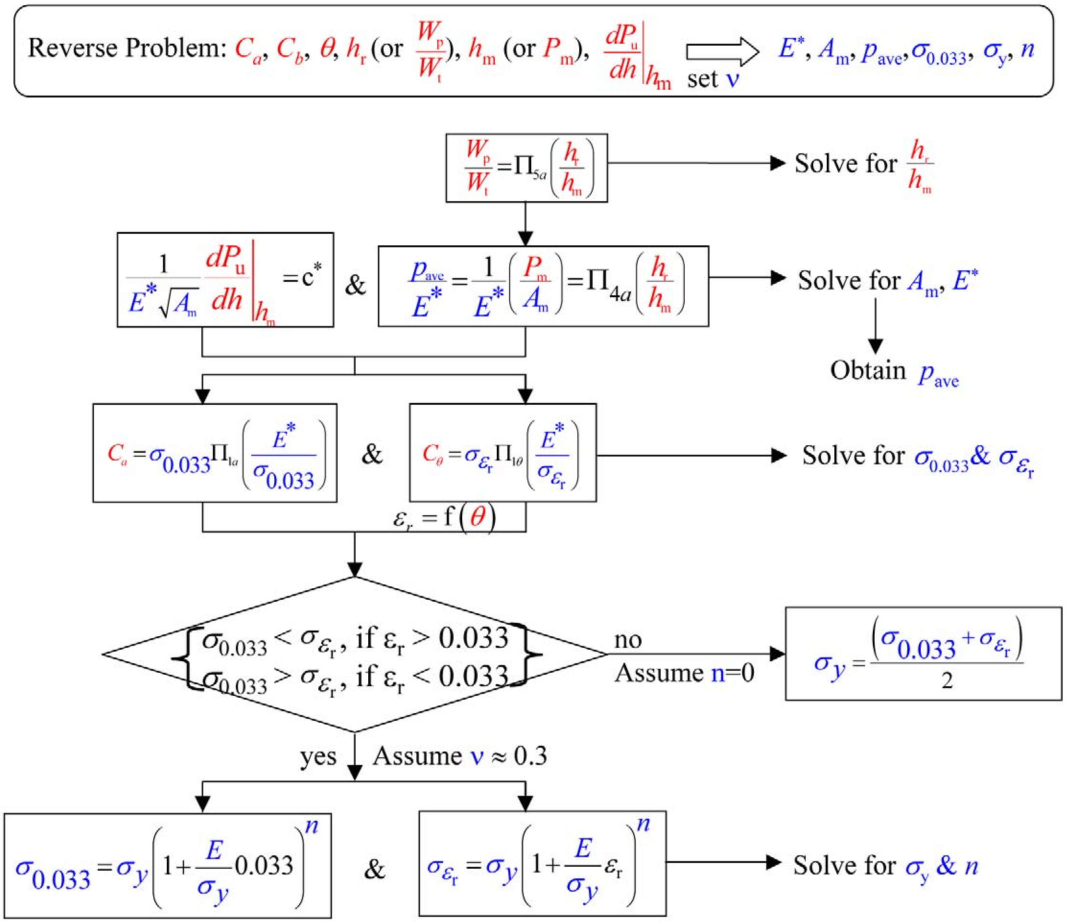

Fig. 7. Dual indentation reverse analysis algorithms.

uniqueness issues by showing that multiple stress–strain curves could result in a visually similar loading and unloading curve. However, such cases were based on the FEM results of 68° apex angle. Following an approach similar to that in Cheng and Cheng [20] for our FEM results of 70.3° apex angle, Fig. 8 shows a set of three visually similar FEM indentation responses of steel with different yield strength and strain hardening exponent. It is worth noting two points here. First, when these three visually similar FEM indentation responses (small but with finite differences in the *P–h* characteristics) were input into the single indenter reverse algorithm [1], three unique sets of mechanical properties can still be obtained, although the accuracy is sensitive to small experimental scatters. Second, using the second indenter for analysis helps in reducing the non-uniqueness problem and improving the accuracy, as clearly shown by the different loading curvatures of the second indentation response from 60° cone tip. The dual indentation reverse algorithm is thus capable of accurately performing the reverse analysis on these three curves.

5. Sensitivity of the dual indentation analysis

5.1. Sensitivity of the forward analysis

Similar to the sensitivity analysis performed in our previous work [1], a ±5% change in any one

Table 6
Dual Indentation Reverse Analysis on Al 6061-T6511 (assume ν = 0.3)

Al 6061-T6511	Single [1]		Dual (+B_{ave})							
	σ_y (MPa)	%err σ_y	E^* (GPa)	%err E^*	$\sigma_{0.033}$ (MPa)	%err $\sigma_{0.033}$	$\sigma_{0.057}$ (MPa)	%err $\sigma_{0.057}$	σ_y (MPa)	%err σ_y
Test A1	333.1	17.3	67.6	−3.7	334.5	−1.0[a]	353.9	0.7	261.7	−7.9
Test A2	349.4	23.0	66.1	−5.8	349.4	3.4	355.3	1.1	322.7	13.6
Test A3	332.8	17.2	66.5	−5.3	332.8	−1.5	355.0	1.0	246.5	−13.2
Test A4	171.0	−39.8	75.0	6.8	322.9	−4.5	348.0	−1.0	225.2	−20.7
Test A5	128.0	−54.9	77.8	10.8	315.9	−6.5	346.0	−1.6	204.4	−28.0
Test A6	278.5	−1.9	67.9	−3.4	337.4	−0.2	353.7	0.6	272.9	−3.9
Average	265.5		70.1		332.1		352.0		255.6	
Uniaxial Exp	284		70.2		338		351.6		284	
STDEV[b]	87.7		4.5		12.2		3.6		47.1	
STDEV/X_{exp}	30.9%		6.5%		3.6%		1.0%		16.6%	

[a] All errors were computed as $X_{\text{rev. analysis}}-\overline{X}_{\text{exp}}/\overline{X}_{\text{exp}}$, where X represents a variable.

[b] STDEV = $\sqrt{\frac{1}{N}\Sigma_{i=1}^{N}(X_{\text{rev. analysis}}-\overline{X}_{\text{exp}})^2}$, where X represents a variable.

Table 7
Dual indentation reverse analysis on Al 7075-T651 (assume ν = 0.3)

Al 7075-T651	Single		Dual (+B_{ave})							
	σ_y (MPa)	%err σ_y	E^* (GPa)	%err E^*	$\sigma_{0.033}$ (MPa)	%err $\sigma_{0.033}$	$\sigma_{0.057}$ (MPa)	%err $\sigma_{0.057}$	σ_y (MPa)	%err σ_y
Test A1	320.2	−36.0	79.5	0.5	537.6	−12.9[a]	585.2	−10.5	380.4	−12.3
Test A2	314.6	−37.1	81.5	−2.6	566.9	−8.2	581.9	−11.0	511.1	−26.7
Test A3	332.1	−33.6	77.2	0.8	557.6	−9.7	589.4	−9.8	447.8	−9.1
Test A4	289.7	−42.1	79.7	2.8	536.8	−13.1	584.9	−10.5	376.7	2.4
Test A5	316.0	−36.8	78.0	4.4	542.5	−12.1	587.8	−10.1	390.1	8.0
Test A6	279.7	−44.1	80.0	4.2	545.4	−11.7	584.5	−10.6	410.3	23.8
Average	308.7		79.3		547.8		585.6		419.4	
Uniaxial exp	500		73.4		617.5		653.6		500	
STDEV[b]	192.14		6.1		70.6		68.0		93.5	
STDEV/X_{exp}	38.4%		8.3%		11.4%		10.4%		18.7%	

[a] All errors were computed as $X_{\text{rev. analysis}}-\overline{X}_{\text{exp}}/\overline{X}_{\text{exp}}$, where X represents a variable.

[b] STDEV = $\sqrt{\frac{1}{N}\Sigma_{i=1}^{N}(X_{\text{rev. analysis}}-\overline{X}_{\text{exp}})^2}$, where X represents a variable.

input parameter (i.e., E^*, σ_y or n) would lead to variations of less than ±7.6% in the predicted results $\left(C_a, \frac{h_r}{h_m}, \left.\frac{dP_u}{dh}\right|_{h_m} \text{ and } C_b\right)$. The rather small variability confirms the robustness of the forward algorithm.

5.2. Sensitivity of the reverse analysis

The sensitivity of the estimated mechanical properties to variations in the input parameters obtained from dual P–h curves was investigated for the 76 cases examined in this study. For each of these cases, the sensitivity of the estimated elasto-

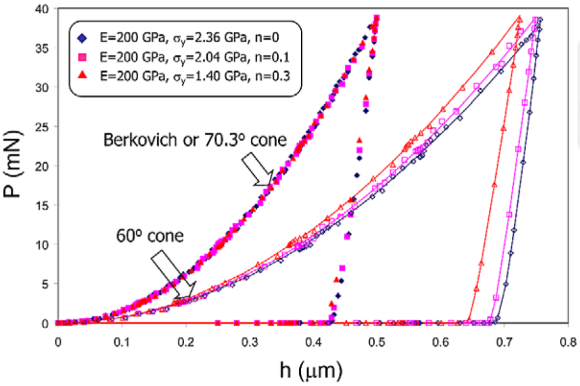

Fig. 8. Dual indentation forward analysis algorithms.

plastic properties to variations in the four P–h curve parameters—C_a, $\left.\frac{dP_u}{dh}\right|_{h_m}$, $\frac{W_p}{W_t}$ and C_b—about their respective reference values (as estimated from the forward analysis) was analyzed. The variations of ±1%, ±2%, ±3% and ±4% in C_a, $\left.\frac{dP_u}{dh}\right|_{h_m}$, $\frac{W_p}{W_t}$ and C_b about their forward prediction values were fed into the reverse algorithm. The outputs from reverse algorithm were statistically compared with the original values of elasto-plastic properties. The standard deviations (STDEV) were calculated for each ±x% variation, thus sampled over 2 × 76 = 152 data points, and compared with that of single indentation. Table 8 lists the specific values of STDEV of the dual indentation normalized with that of the single indentation at ±2% C_a, ±2% $\left.\frac{dP_u}{dh}\right|_{h_m}$ and ±1% $\frac{W_p}{W_t}$, typically found in the experimental scattering. Other variations in the P–h curve parameters follow the similar trend shown in Table 8. Significant improvement of yield strength (for a two-parameter power law plastic constitutive law) was achieved due to the second plasticity parameter, $\sigma_{0.057}$, which can be predicted as robustly as $\sigma_{0.033}$. For instance, within ±1% experimental error in W_p/W_t, the average error in the estimated yield strength was reduced by 80% using the dual indentation algorithm.

Table 8
Normalized standard deviations in properties estimation using dual indentation reverse algorithm

(Output) change in \ (Input) change in		±2% C_a	±2% $\left.\frac{dP_u}{dh}\right\|_{h_m}$	±1% W_p/W_t
Normalized STDEV in estimated properties[a]	E^*	1	1	1
	$\sigma_{0.033}$	1	1	1
	σ_y ($n \le 0.1$)	1	0.45	0.20
	σ_y ($n > 0.1$)	0.83	0.34	0.18
	p_{ave}	1	1	0.53

[a] The normalized STDEV is calculated from $\mathrm{STDEV}_{dual}/\mathrm{STDEV}_{single}$, where $\mathrm{STDEV} = \sqrt{\frac{1}{N}\Sigma_{i=1}^{N}(X_{\mathrm{varied}} - X_{\mathrm{reference}})^2}$ and X_{varied} represents a percentage deviation from $X_{\mathrm{reference}}$.

6. Extension to multiple-indentation analysis

To further improve the accuracy and reduce the sensitivity of the reverse algorithm, multiple indenter geometries may be used. This multiple indentation analysis requires a complete indentation curve of Vickers/Berkovich indenter and a loading indentation curve of other tip geometries, $\theta \in [50°,80°]$. A set of the multiple indentation reverse algorithms is shown in Fig. 9. It is similar to that of dual indentation except at the last step where yield strength and strain hardening exponent are to be determined. For each indenter geometry (θ), a pair of representative strain and stress can be determined using generalized dimensionless function $\Pi_{1\theta}$ and $\varepsilon_{r\theta}$ in Eqs. (A.10) and (10a,b), respectively. By statistically fitting (least square error) these stress/strain values with the power hardening equation (Eq. (4)), σ_y and n can be determined.

On the other hand, the dual indentation algorithms shown in Fig. 6 can be easily extended to different tip geometries $\theta \in [50°,80°]$. Given a set of elasto-plastic properties, one can predict a complete indentation response for Vickers/Berkovich indenter and a loading indentation response for arbitrary indenter tip geometries.

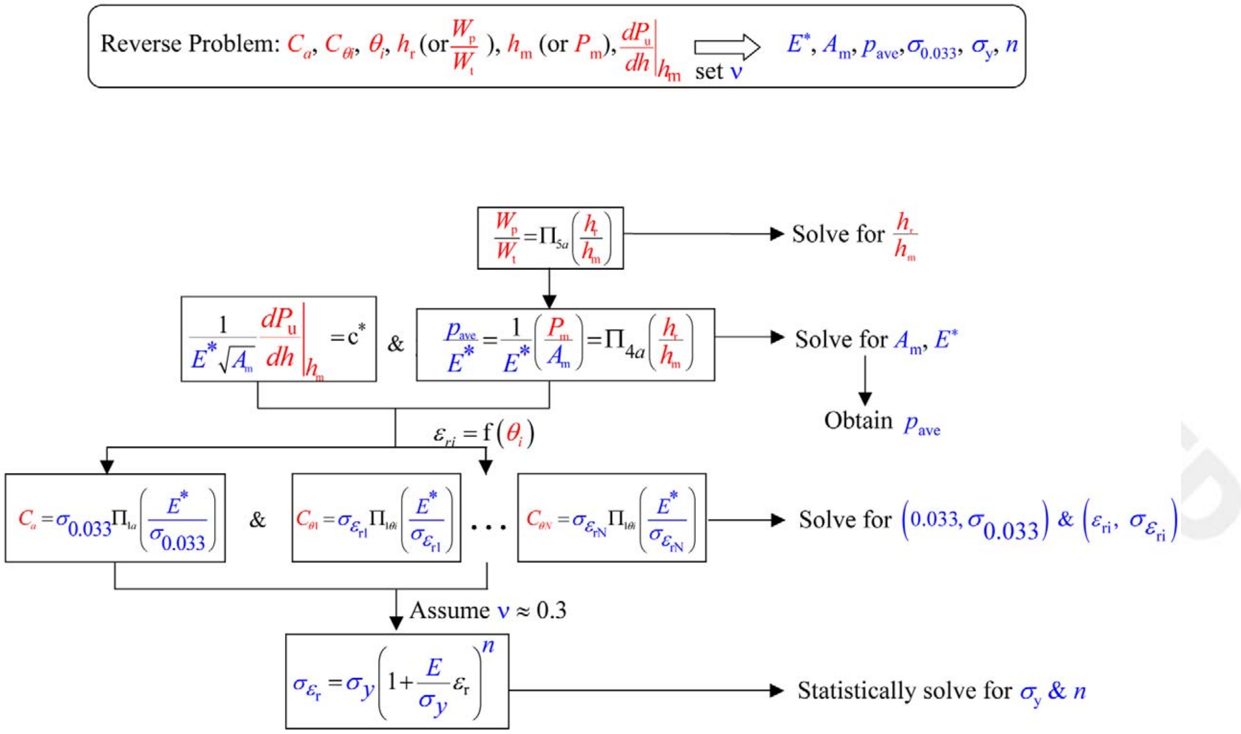

Fig. 9. Multiple indentation reverse analysis algorithms.

7. Conclusions

In this study, dimensional analyses and large deformation finite element studies were performed to address the uniqueness problem in the extraction of material properties from instrumented sharp indentation and to improve the accuracy and sensitivity of the algorithms used to extract such properties. The key results of this investigation can be summarized as follows:

1. Using dimensional analysis, additional universal, dimensionless functions were constructed to correlate elasto-plastic properties of materials with indentation response for 50°, 60° and 80° cone (or their equivalent 3-sided pyramids). Choosing a pair of Berkovich (or Vickers) and 60° cone (or its equivalent 3-sided pyramid), forward and reverse analysis algorithms were established based on the identified dimensionless functions. These algorithms allow for the calculation of indentation response for a given set of properties, and also for extraction of some plastic properties from a dual set of indentation data, thus obviating the need for large-scale finite element computations after each indentation test.
2. Assuming large deformation FEM simulations and an isotropic power law elasto-plastic constitutive description within the specified range of material parameters, the present reverse algorithms using dual indenters (Berkovich/Vickers and cone of 60° apex angle) were able to predict a single set of values for E^*, σ_y and n. Furthermore, the full stress–strain response can be estimated from the power law assumption.
3. The accuracy of the dual indentation forward/reverse algorithms were verified in two aluminum alloys (6061-T6511 and 7075-T651) with an improvement over the single indentation forward/forward algorithms.
4. The proposed dual indentation forward algorithms work well and robustly with similar sensitivity to the single indentation forward algor-

ithms; a ±5% error in any input parameter results in less than ±7.6% in the predicted values of $C_a, \frac{h_r}{h_m}, \left.\frac{dP_u}{dh}\right|_{h_m}$ or C_b.

5. The proposed dual indentation reverse algorithms were found to predict E^*, $\sigma_{0.033}$ and $\sigma_{0.057}$ quite well, and σ_y reasonably well for the cases studied. Comprehensive sensitivity analyses show that σ_y displayed much reduced sensitivity to all P–h parameters due to the second plasticity parameter that can be robustly estimated; whereas, E^*, $\sigma_{0.033,}$ $\sigma_{0.057}$ and p_{ave} displayed similar sensitivity to the single indentation algorithms.
6. The extension of forward/reverse algorithms to using multiple indenter geometries, $50° \leq \theta \leq 80°$, was proposed with generalized functions of representative strain and indentation loading curvature.

Acknowledgements

This research was supported by the Defense University Research Initiative on Nano-Technology (DURINT) on "Damage and Failure Resistant Nanostructured Materials" which is funded at MIT by the Office of Naval Research, Grant No. N00014-01-1-0808 and by a subcontract to MIT through the Center for Thermal Spray Research at Stony Brook, under the National Science Foundation Grant DMR-0080021. A special note of thanks is extended to Dr. Krystyn van Vliet and Dr. Jim Smith for their helps in conducting the experiments reported here.

Appendix A

In this appendix, eight dimensionless functions used in the current study are listed. Π_{1a},Π_{2a},Π_{3a},Π_{4a},Π_{5a},Π_{6a} were constructed in our earlier work [1], and Π_{1b},Π_{1c} and Π_{1d} are constructed in the current study. These functions can be used to formulate dual indentation forward and reverse algorithms in addition to single indentation algorithms.

$$\Pi_{1a} = \frac{C_a}{\sigma_{0.033}} = -1.131\left[\ln\left(\frac{E^*}{\sigma_{0.033}}\right)\right]^3 + 13.635\left[\ln\left(\frac{E^*}{\sigma_{0.033}}\right)\right]^2 - 30.594\left[\ln\left(\frac{E^*}{\sigma_{0.033}}\right)\right] + 29.267 \tag{A.1}$$

$$\Pi_{2a}\left(\frac{E^*}{\sigma_{0.033}},n\right) = \frac{1}{E^* h_m}\left.\frac{dP_u}{dh}\right|_{h_m} = (-1.40557n^3 + 0.77526n^2 + 0.15830n - 0.06831)\left[\ln\left(\frac{E^*}{\sigma_{0.033}}\right)\right]^3 + (17.93006n^3 - 9.22091n^2 - 2.37733n + 0.86295)\left[\ln\left(\frac{E^*}{\sigma_{0.033}}\right)\right]^2 + (-79.99715n^3 + 40.55620n^2 + 9.00157n - 2.54543)\left[\ln\left(\frac{E^*}{\sigma_{0.033}}\right)\right] + (122.65069n^3 - 63.88418n^2 - 9.58936n + 6.20045) \tag{A.2}$$

$$\Pi_{3a}\left(\frac{\sigma_{0.033}}{E^*},n\right) = \frac{h_r}{h_m} = (0.010100n^2 + 0.0017639n - 0.0040837)\left[\ln\left(\frac{\sigma_{0.033}}{E^*}\right)\right]^3 + (0.14386n^2 + 0.018153n - 0.088198)\left[\ln\left(\frac{\sigma_{0.033}}{E^*}\right)\right]^2 + (0.59505n^2 + 0.034074n - 0.65417)\left[\ln\left(\frac{\sigma_{0.033}}{E^*}\right)\right] + (0.58180n^2 - 0.088460n - 0.67290) \tag{A.3}$$

$$\Pi_{4a} = \frac{p_{ave}}{E^*} \approx 0.268536\Big(0.9952495 \tag{A.4}$$

$$-\frac{h_r}{h_m}\bigg)^{1.1142735}$$

$$\Pi_{5a} = \frac{W_\mathrm{p}}{W_\mathrm{t}} = 1.61217\bigg\{1.13111$$

$$-1.74756\Big[^{-1.49291\left(\frac{h_\mathrm{r}}{h_\mathrm{m}}\right)^{2.535334}}\Big] \tag{A.5}$$

$$-0.075187\left(\frac{h_\mathrm{r}}{h_\mathrm{m}}\right)^{1.135826}\bigg\}$$

$$\Pi_{6a} = \frac{1}{E^*\sqrt{A_\mathrm{m}}}\frac{\mathrm{d}P_\mathrm{u}}{\mathrm{d}h}\bigg|_{h_\mathrm{m}} = c^* \tag{A.6}$$

where values of c^* are tabulated in Table A.1.

For $\theta = 60°$,

$$\Pi_{1b} = \frac{C_b}{\sigma_{0.057}} = -0.154\left[\ln\left(\frac{E^*}{\sigma_{0.057}}\right)\right]^3$$

$$+0.932\left[\ln\left(\frac{E^*}{\sigma_{0.057}}\right)\right]^2 + 7.657\left[\ln\left(\frac{E^*}{\sigma_{0.057}}\right)\right] \tag{A.7}$$

$$-11.773$$

For $\theta = 80°$,

$$\Pi_{1c} = \frac{C_c}{\sigma_{0.017}} = -2.913\left[\ln\left(\frac{E^*}{\sigma_{0.017}}\right)\right]^3$$

$$+44.023\left[\ln\left(\frac{E^*}{\sigma_{0.017}}\right)\right]^2 \tag{A.8}$$

$$-122.771\left[\ln\left(\frac{E^*}{\sigma_{0.017}}\right)\right] + 119.991$$

For $\theta = 50°$,

$$\Pi_{1d} = \frac{C_d}{\sigma_{0.082}} = 0.0394\left[\ln\left(\frac{E^*}{\sigma_{0.082}}\right)\right]^3$$

$$-1.098\left[\ln\left(\frac{E^*}{\sigma_{0.082}}\right)\right]^2 + 9.862\left[\ln\left(\frac{E^*}{\sigma_{0.082}}\right)\right] \tag{A.9}$$

$$-11.837$$

For any θ in [50°,80°], the general fit function for $\Pi_{1\theta}$ is

$$\Pi_{1\theta} = \frac{C_\theta}{\sigma_{\varepsilon_\mathrm{r}}} = (-2.3985\times10^{-5}\theta^3$$

$$+6.0446\times10^{-4}\theta^2 + 0.132443\theta$$

$$-5.0950)\left[\ln\left(\frac{E^*}{\sigma_{\varepsilon_\mathrm{r}}}\right)\right]^3 + (0.0014741\theta^3$$

$$-0.21502\theta^2 + 10.4415\theta$$

$$-169.8767)\left[\ln\left(\frac{E^*}{\sigma_{\varepsilon_\mathrm{r}}}\right)\right]^2 + (-3.9124 \tag{A.10}$$

$$\times10^{-3}\theta^3 + 0.53332\theta^2 - 23.2834\theta$$

$$+329.7724)\left[\ln\left(\frac{E^*}{\sigma_{\varepsilon_\mathrm{r}}}\right)\right] + (2.6981$$

$$\times10^{-3}\theta^3 - 0.29197\theta^2 + 7.5761\theta$$

$$+2.0165)$$

Table A.1
The values of $c*$ used in the study [1]

$c*$	Small deformation linear elastic solution[a]	Large deformation elasto-plastic solution[b]
Conical	1.128	1.1957
Berkovich	1.167	1.2370
Vickers	1.142	1.2105

[a] King [29].
[b] Proposed in the current study.

Appendix B

In this study, large deformation finite element computational simulations of depth-sensing indentation were carried out for 76 different combinations of elasto-plastic properties that encompass the wide range of parameters commonly found in pure and alloyed engineering metals; Young's modulus, E, was varied from 10 to 210 GPa, yield strength, σ_y, from 30 to 3000 MPa, and strain hardening exponent, n, from 0 to 0.5, and the Poisson's ratio, ν, was fixed at 0.3. Table B.1 tabulates the elasto-plastic parameters used in these 76 cases.

Table B.1
Elasto-plastic parameters used in the present study

	E (GPa)	σ_y (MPa)	σ_y/E
19 combinations of E and σy[a]	10	30	0.003
	10	100	0.01
	10	300	0.03
	50	200	0.004
	50	600	0.012
	50	1000	0.02
	50	2000	0.04
	90	500	0.005556
	90	1500	0.016667
	90	3000	0.033333
	130	1000	0.007692
	130	2000	0.015385
	130	3000	0.023077
	170	300	0.001765
	170	1500	0.008824
	170	3000	0.017647
	210	300	0.001429
	210	1800	0.008571
	210	3000	0.014286

[a] For each one of the 19 cases listed above, strain hardening exponent n is varied from 0, 0.1, 0.3 to 0.5, resulting in a total of 76 different cases.

References

[1] Dao M, Chollacoop N, Van Vliet KJ, Venkatesh TA, Suresh S. Acta Mater 2001;49:3899.
[2] Tabor D. Hardness of metals. Oxford: Clarendon Press, 1951.
[3] Tabor D. Rev Phys Technol 1970;1:145.
[4] Doener MF, Nix WD. J Mater Res 1986;1:601.
[5] Pharr GM, Cook RF. J Mater Res 1990;5:847.
[6] Oliver WC, Pharr GM. J Mater Res 1992;7:1564.
[7] Field JS, Swain MV. J Mater Res 1993;8:297.
[8] Field JS, Swain MV. J Mater Res 1995;10:101.
[9] Gerberich WW, Nelson JC, Lilleodden ET, Anderson P, Wyrobek JT. Acta mater 1996;44:3585.
[10] Bolshakov A, Oliver WC, Pharr GM. J Mater Res 1997;11:760.
[11] Alcala J, Giannakopoulos AE, Suresh S. J Mater Res 1998;13:1390.
[12] Cheng YT, Cheng CM. J Appl Phys 1998;84:1284.
[13] Cheng YT, Cheng CM. Appl Phys Lett 1998;73:614.
[14] Suresh S, Nieh T-G, Choi BW. Scripta Mater 1999;41:951.
[15] Gouldstone A, Koh H-J, Zeng K-L, Giannakopoulos AE, Suresh S. Acta mater 2000;48:2277.
[16] Johnson KL. J Mech Phys Solids 1970;18:115.
[17] Suresh S, Alcala J, Giannakopoulos AE. US Patent No. 6,134,954, Date of Issue: October 24, 2000.
[18] Dao M, Chollacoop N, Van Vliet KJ, Venkatesh TA, Suresh S. US Provisional Patent, filed with the US Patent Office on March 7, 2001.
[19] Giannakopoulos AE, Larsson P-L, Vestergaard R. Int J Solids Struct 1994;31:2679.
[20] Cheng YT, Cheng CM. J Mater Res 1999;14:3493.
[21] Giannakopoulos AE, Suresh S. Scripta Mater 1999;40:1191.
[22] Venkatesh TA, Van Vliet KJ, Giannakopoulos AE, Suresh S. Scripta Mater 2000;42:833.
[23] Suresh S, Giannakopoulos AE. Acta Mater 1998;46:5755.
[24] Tunvisut K, O'Dowd NP, Busso EP. Int J Solids Struct 2001;38:335.
[25] Hill R, Storakers B, Zdunek AB. Proc R Soc Lond 1989;A423:301.
[26] Larsson P-L, Giannakopoulos AE, Soderlund E, Rowcliffe DJ, Vestergaard R. Int J Solids Struct 1996;33:221.
[27] Johnson KL. Contact mechanics. London: Cambridge University Press, 1985.
[28] ABAQUS theory manual version 6.1, Pawtucket: Hibbitt, Karlsson and Sorensen, Inc., 2000.
[29] King RB. Int J Solids Struct 1987;23:1657.